CAMBRIDGE
UNIVERSITY PRESS

RESEARCH ARTICLE

Evaluation of a machine-learning-driven active–passive upper-limb exoskeleton robot: Experimental human-in-the-loop study

Ali Nasr[1] , Jason Hunter[1], Clark R. Dickerson[2] and John McPhee[1]

[1]Systems Design Engineering, University of Waterloo, Waterloo, ON N2L 3G1, Canada
[2]Kinesiology and Health Sciences, University of Waterloo, Waterloo, ON N2L 3G1, Canada
Corresponding author: Ali Nasr; Email: a.nasr@uwaterloo.ca

Abstract

Evaluating exoskeleton actuation methods and designing an effective controller for these exoskeletons are both challenging and time-consuming tasks. This is largely due to the complicated human–robot interactions, the selection of sensors and actuators, electrical/command connection issues, and communication delays. In this research, a test framework for evaluating a new active–passive shoulder exoskeleton was developed, and a surface electromyography (sEMG)-based human-robot cooperative control method was created to execute the wearer's movement intentions. The hierarchical control used sEMG-based intention estimation, mid-level strength regulation, and low-level actuator control. It was then applied to shoulder joint elevation experiments to verify the exoskeleton controller's effectiveness. The active–passive assistance was compared with fully passive and fully active exoskeleton control using the following criteria: (1) post-test survey, (2) load tolerance duration, and (3) computed human torque, power, and metabolic energy expenditure using sEMG signals and inverse dynamic simulation. The experimental outcomes showed that active–passive exoskeletons required less muscular activation torque (50%) from the user and reduced fatigue duration indicators by a factor of 3, compared to fully passive ones.

1. Introduction

A wearable exoskeleton interacts with the human body's structure (Nasr et al., 2021c). Its potential applications include rehabilitating patients, developing motor skills, boosting human performance, and decreasing muscle fatigue (Nasr et al., 2021c; Gillette et al., 2022; Nasr et al., 2022a). However, safe and effective exoskeleton control is a challenging problem (Nasr et al., 2021c). Challenges include human–robot interaction (HRI), human-in-the-loop (HITL) control, physiological signal interpretation, actuation type, and real-time application. So far, most issues, except real-time tests, have been studied in offline analysis (Fritzsche et al., 2021). The challenges of real-time application may require special tools, methods, and parameters.

Modern exoskeleton, prosthetic, assistive, and rehabilitation robot controls follow a hierarchical structure with control laws at the high, middle, and low levels (Young and Ferris, 2017; du Plessis et al., 2021; Nasr et al., 2022b). The high-level controller deciphers the user's motion intent or user wrench

CrossMark

(torque/force). The most popular technique for testing and managing wearable exoskeleton robots and bionic prostheses is the interpretation of biological signals (Nasr et al., 2021a). The brain produces biological signals and sends them to muscles as action potentials, so that the body is moved and controlled. The most frequently applied physiological signals that are utilized to analyze human movement and rehabilitation are surface electromyography (sEMG; Yun et al., 2020; Nasr et al., 2021a) signals. Biological signal interpretation or classification was successfully achieved using machine-learning methods (Nasr et al., 2021a), primarily using offline analysis. However, as a result of safety concerns, real-time sEMG-based machine-learning-driven robots have not been widely utilized.

The mid-level controller converts the high-level controller's intended motion or wrench into the low-level controller's desired trajectory of motion or wrench. The assist-as-needed (AAN)-computed-torque method (CTM approach for the mid-level controller, which relies on augmenting rather than substituting motor effort, has shown encouraging outcomes (Gull et al., 2020; Yihun et al., 2020; Asl et al., 2021; Wang et al., 2021; Nasr et al., 2022b). So far, this mid-level controller has been tested in simulation studies. Although a comprehensive and verified model may be used for controller design (Nasr et al., 2022b), it is essential to test the controller in HITL experiments.

The low-level unit is in charge of instructing the robotic actuators to follow the desired states (commanded by the mid-level unit), while taking into account the measured states (from the sensors) (Young and Ferris, 2017; du Plessis et al., 2021). Designing and tuning gains of a low-level controller does not happen within a simulation and requires understanding and evaluating the actuator, physical system, power transmission system, control delays, and computational challenges. We aim to adjust the low-level controller gain by means of verbal feedback from the participants interacting with the exoskeleton.

The exoskeleton design is divided into three actuation categories: fully passive, fully active, and active–passive. A fully passive mechanism usually stores potential energy from human motion (de Looze et al., 2016; Nasr et al., 2022a). Compared to other categories, it is less sophisticated in terms of sensing and control, and it is portable, safe, economical, and requires fewer maintenance (de Looze et al., 2016; de Vries and de Looze, 2019; Nasr et al., 2022a). Instead of supplying an assistive torque as a fixed function of joint angle (fully passive), active (powered) exoskeletons supply torque as a variable function of time or states using actuators such as an electric motor, a hydraulic cylinder, or a pneumatic artificial muscle (de Looze et al., 2016; Gopura et al., 2016). Since the entire torque source of the exoskeleton depends on an active component, the energy source, and the used actuator must be powerful. As a result, active (powered) exoskeletons are big, heavy, fixed in place, expensive, and have a low power-to-weight ratio (Bogue, 2018).

Some technologies combine active and passive power transmissions to reduce the drawbacks of fully active and fully passive exoskeletons (Naito et al., 2007; Matthew et al., 2015; Otten et al., 2018; Al-Hayali et al., 2021a, 2021b; Miakovic et al., 2022). Passive mechanisms serve to minimize the size, weight, and necessary active torque, which in turn improves portability (Smith et al., 2013; Blanchet et al., 2020; Miakovic et al., 2022). Recently, the semi-active, semi-passive, and quasi-passive nature of this combined transmission system has been conceptually investigated on lower limbs (Lambrecht and Kazerooni, 2009; Hassan and Sadik, 2018; Di Natali et al., 2020; Pillai et al., 2020; Al-Hayali et al., 2021a, 2021b; Ren et al., 2021; Wang et al., 2021), upper limbs (Naito et al., 2007; Smith et al., 2013; Zahedi et al., 2021; Bai et al., 2022; Winter et al., 2022), and spines (Jamsek et al., 2020). However, from a practical point of view, it is necessary to consider the HRI, as well as control delays in regulating the active component of this integrated system. Our goal is to assess and contrast a fully passive, fully active, and active–passive shoulder exoskeleton in an experimental study for the first time.

Exoskeleton power transmission sources must be assessed using various criteria that consider both human and robot systems. To the best of our knowledge, the literature has not offered specific instructions for evaluating active–passive systems in the HRI experiment. The primary goal of this project is to develop a practical test for hierarchical control of an upper-limb exoskeleton designed for a particular worker or patient. The secondary goal of this project is to reduce user effort by tuning the control gains and selecting the correct strength level of the passive mechanism. Participants who were engaged with the robot provided the data for evaluation.

The following is a list of the research contributions:

   I. Implementing a hierarchical scheme for real-time sEMG-based control of a shoulder exoskeleton.
  II. Evaluating active–passive in HITL experiments assistance and comparing it with fully passive and fully active exoskeletons using the following criteria: (1) post-test survey, (2) load tolerance duration, (3) mean power frequency, (4) motion fatigue, and (5–8) computed human active torque, joint torque, power, and metabolic energy expenditure using an experimentally validated and scalable neuromusculoskeletal (NMSK) model.
 III. Suggesting current real-time implementation challenges to address in future offline studies and analysis.

First, the required equipment, calibration steps, and data preparation are introduced in Section 2. Second, hierarchical schemes are introduced, modeled, and implemented (Section 3). Third, test protocol and phases, as well as the exoskeleton evaluation criteria, are introduced in Sections 4 and 5. Finally, the results for different criteria are presented, compared, and discussed in Section 6.

2. Equipment

Here, the wearable passive device, the augmented active component, the sensors, and the connection protocols/methods used to assess the performance of the active–passive exoskeleton robot, are introduced.

2.1. Shoulder exoskeleton

We have added a motor to an EVO (Ekso Bionics Holdings Inc, California, USA) upper-limb exoskeleton with built-in passive assistance (Figure 1(a)). The method of combining active and passive components can be applied to any upper-limb exoskeleton. The EVO upper-limb exoskeleton has 1-degree of freedom (DoF) for each side (left and right) of the shoulder elevation joint that rotates with a passive mechanism. Level 1, 2, and 3 springs provide a maximum torque of 4.578, 7.693, and 9.798Nm, respectively. The exoskeleton passive joint is attached to a hip belt using passive accordion-like joints and links that allow movement in the horizontal plane. The exoskeleton armrest attaches to the user's upper arm. The exoskeleton was modeled, including its passive torque-angle function, and validated in Nasr et al. (2023a).

2.2. Motor and encoder

An AK80–9 KV100 brushless direct current (BLDC) motor (Cubemars, Jiangxi Xintuo Enterprise Co., China) with the properties in Table 1 has been used for the active component. The built-in motor driver communicates with controllers through a controller area network (CAN-bus) and calibrates through serial communication.

    The actuators driver board utilizes a field-oriented control (FOC) unit and is supplied with an active disturbance rejection control loop to control the speed and angle, according to Figure 2. This low-level controller is responsible for rejecting disturbances and applying the desired kinematics and kinetics that are commanded by the mid-level controller. This low-level controller consists of proportional-derivative feedback and a torque feed-forward controller. In total, five variables should be commanded to the built-in controller via CAN-bus from MATLAB. These five variables are desired angular position (ϕ_{ref}), desired angular velocity ($\dot{\phi}_{ref}$), feed-forward desired torque (T_r), proportional gain (K_p), and derivative gain (K_d).

    We have designed an intermediary adaptor to connect MATLAB to the motor using an Arduino Uno and a CAN-bus Shield V2.0 (Seeed Technology Inc, Shenzhen, China). MATLAB connects to the Arduino with a serial communication port ($115200 \frac{\text{bits}}{\text{s}}$). The Arduino converts the received string to an integer for commanding the motor. To increase the robustness of the conveyed data, the data that consists
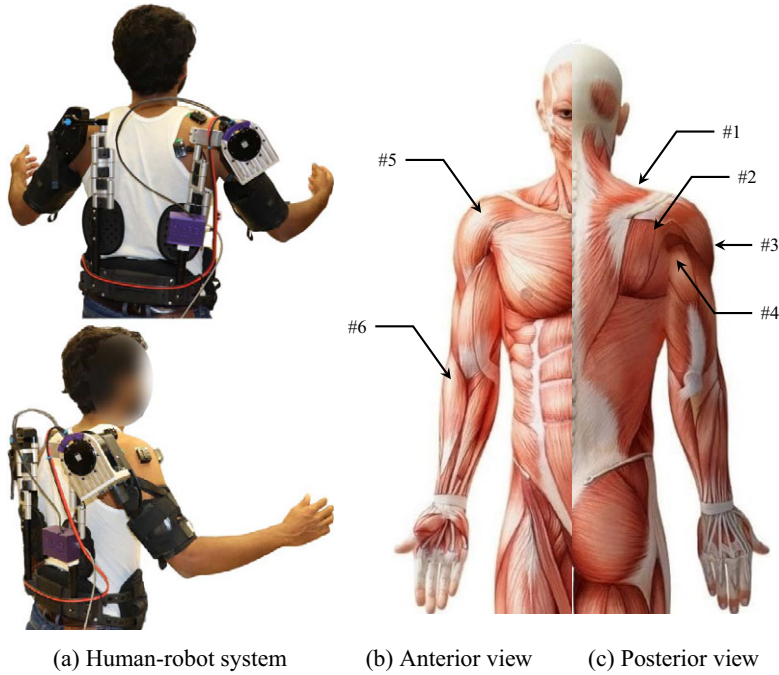
(a) Human-robot system   (b) Anterior view   (c) Posterior view

Figure 1. *(a) Depiction of a healthy subject wearing an actual EVO passive system with an augmented BLDC motor on the elevation joint. (c & d) The depiction of the sEMG electrode and IMU placements using Delsys Trigno wireless sEMG system (Delsys Inc, Natick, MA, USA), over the area of #1 UTRA, #2 MTRA, #3 MDEL, #4 PDEL, #5 ADEL, and #6 BRD of the right forearm, shoulder, and upper trunk muscles.*

Table 1. *The properties of the AK80–9 KV100 BLDC motor (Cubemars, Jiangxi Xintuo Enterprise Co., China)*

	Physical				Electrical								Ratios				Driver				
Weight (kg)	Outside diameter (m)	Height (m)	Number of pole-pair	Voltage (V)	Rated torque (Nm)	Peak torque (Nm)	Max output speed at rated torque (rpm)	Rated current (A)	Peak current (A)	Resistance phase to phase (*m*)	Inductance phase to phase (uH)	Kt (Nm/A)	Kv (rpm/V)	Ke (V/rpm)	Km ($Nm/w^{0.5}$)	Max torque weight ratio (Nm/kg)	Gear reduction ratio	Rated voltage (V)	Rated current (A)	Current consumption (mA)	CAN-bus bit rate (Mbps)	Working environment temperature (C)	Absolute encoder accuracy (bit/rev)
.485	0.098	0.0385	21	24	9	18	245	12	24	170	57	0.091	100	0.009524	0.2206	37	9:1	48	20	50	1	-20 - +65	14

of specific start and end frames, as well as fixed length, is given a special pattern. The Arduino connects to the CAN-bus board through a serial peripheral interface (SPI). The CAN-bus board includes an MCP2515 CAN-bus controller and an MCP2551 CAN-bus transceiver.
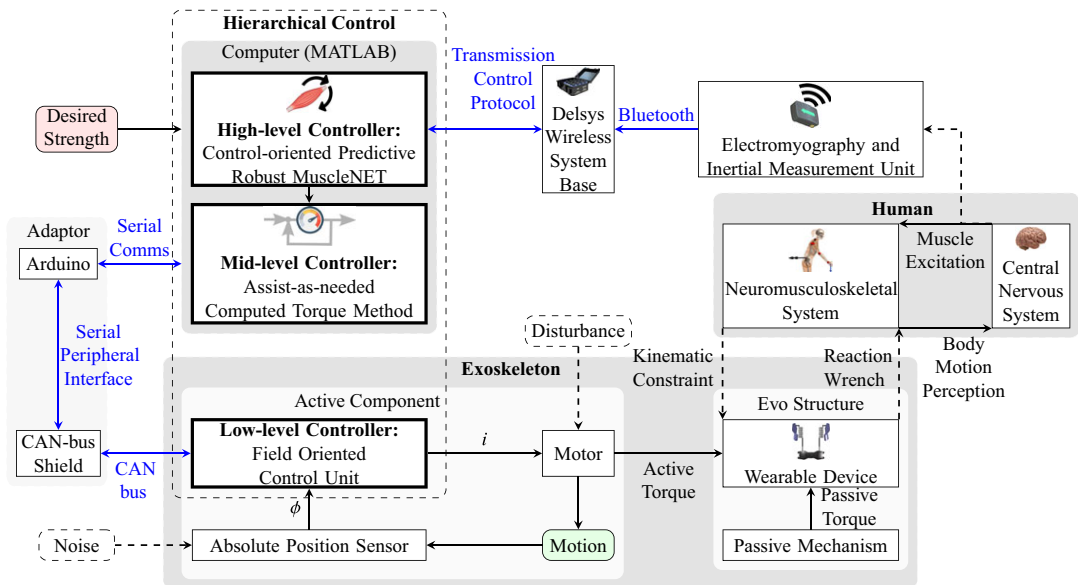
Figure 2. *Block diagram of main control system components and connection protocols. The high, mid, and low-level controllers are described in Section 3. The connection protocols/methods are highlighted as blue arrows.*

2.3. Surface electromyography and inertial measurement unit

For the connection and streaming of real-time data between a computer and a Delsys Trigno wireless sEMG system (Delsys Inc, Natick, MA, USA), the TRIGNO software development toolkit (SDK) has been used. Delsys's wireless system base should be connected to the computer using a USB cable. The transmission control protocol (TCP), a standardized protocol for transmitting information over a network, receives the data from the base and provides the data over a virtual TCP/IP server with the trigno control utility (TCU). The Trigno SDK utilizes five TCP ports to communicate with client applications (Table 2). The TCU application listens for incoming connections and manages data routing to any applications that connect. All sEMG channels stream through the 50043 port, and all additional data channels stream through the 50044 port. Additionally, any sensors with 4 or fewer data channels, or an inertial measurement unit (IMU), will have data duplicated on the 50041 and 50042 ports. A "START" command to the command port or a start trigger to the Trigno base station initiates data acquisition.

As illustrated in Figure 1, sEMG signals were measured from 6 sites over muscles of the right limb and trunk, similar to those suggested by Hislop et al. (2013). The locations are #1 upper trapezius (UTRA), #2

Table 2. *The TCP/IP server 5 port names, numbers, and functions*

| Name | Number | Function | | Sampling | |
		Receives	Sends	Channels	Rate (Hz)	Period (s)
Command	50040	Commands	Replies to control commands	1		
sEMG Data	50043	N/A	sEMG and primary non-sEMG data from all sensor types	16	1111.111	0.0135/15
AUX Data	50044	N/A	Auxiliary non-sEMG data from all sensor types	144	148.148	0.0135/2
Legacy sEMG Data	50041	N/A	sEMG and primary non-sEMG data from select sensor types	16	1925.925	0.0135/26
Legacy AUX Data	50042	N/A	Auxiliary non-sEMG data from select sensor types	48	148.148	0.0135/2
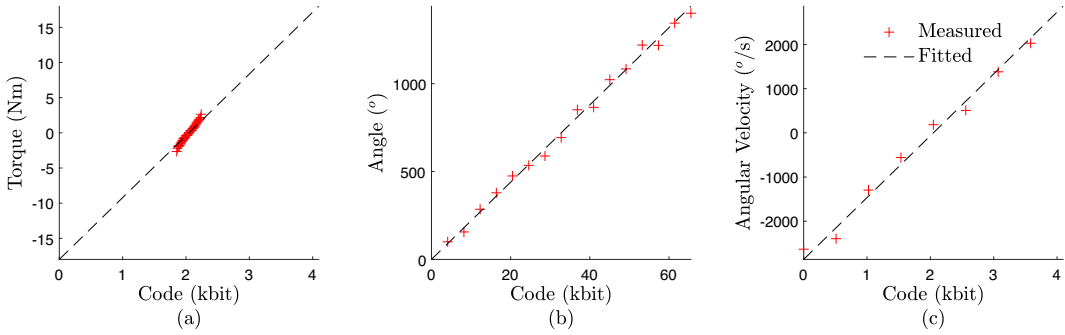
Figure 3. *The motor (a) torque function of code (measured and fitted), (b) the motor angle function of code, (c) the motor velocity function of code.*

middle trapezius (MTRA), #3 middle deltoid (MDEL), #4 posterior deltoid (PDEL), #5 anterior deltoid (ADEL), and #6 brachioradialis (BRD). No sensors were attached to the upper arm area since the exoskeleton armrest covered the area.

2.4. Calibration

The motor command and feedback signals are defined as unsigned integer data, but we have converted them to real numbers using linear regression. The motor angle (ϕ_{ref}), the motor speed ($\dot{\phi}_{ref}$), the FOC proportional gain (K_p), the FOC derivative gain (K_d), and the motor torque (T_{ref}) were defined between 0 and 65535, 4095, 4095, 4095, 4095 bits, respectively. We have mapped the motor torque to the input code using Figure 3(a). According to the manufacturer's manual, the motor absolute position sensor is calibrated for 4 full revolutions (Figure 3(b)). Additionally, the motor speed is calibrated for $\pm 50 \frac{rad}{s}$ (Figure 3(c)).

2.5. Data preparation

The machine-learning model inputs to the high-level controller are the filtered sEMG signals, the Euler angle data from a built-in IMU in the sEMG sensors, and the motor kinematic data. These data are filtered or rectified in the preparation stage, as described below, before feeding to the high-level controller.
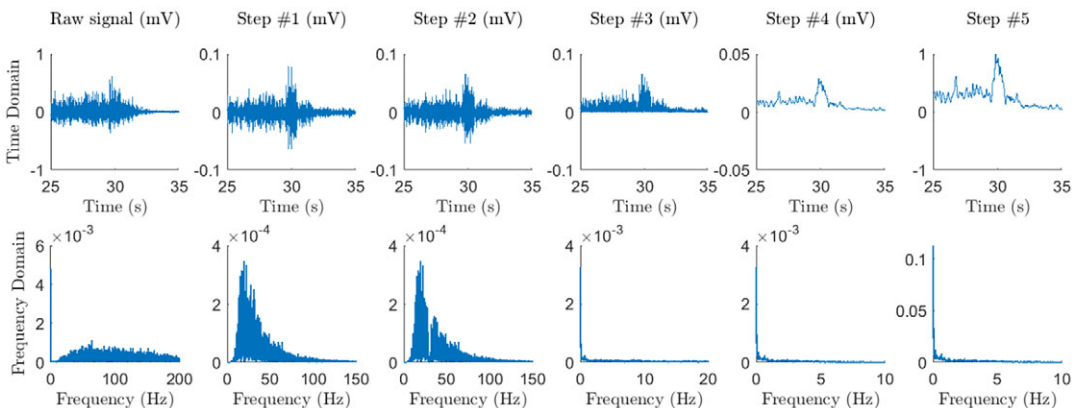

Figure 4. *Raw and filtered sEMG signal samples in the time and frequency domains.*

- **sEMG data:** The raw signals were filtered using the methods described below. A sample of sEMG signals that were filtered is shown in Figure 4. In contrast to a mathematical muscle model, which requires more filtering steps and analysis, these steps are provided for machine-learning mapping electromyography to kinematic and dynamic biomechanical variables (MuscleNET), a machine-learning mapping method.

  Step #1 A band-pass filter with a cutoff frequency of $20 - 500$Hz was applied (Hermens et al., 2000; Drake and Callaghan, 2006) (signals with less than 20Hz frequency were cleaned to remove the motion artifacts, and sEMG signals with frequency more than 500Hz were removed as they had insignificant power spectral density (Reaz et al., 2006)).

  Step #2 A band-stop filter, known as a notch filter, with a cutoff frequency of $55 - 65$Hz was used (to clear the 60Hz noise from the measurement unit).

  Step #3 An absolute function (commonly known as the rectification process of sEMG signals) was used to make the signal positive. This step alters the power spectral density of the recorded signal as shown in Figure 3 (Neto and Christou, 2010; Nasr et al., 2021b).

  Step #4 A low-pass filter with a cutoff frequency of 7Hz (Hermens et al., 2000) was used to smooth the sEMG signal (Nasr et al., 2021b).

  Step #5 A normalization function to the subject's maximum signal amplitude was used.

  Step #6 A re-sampling function using the 1D data cubic interpolation method to a 20Hz rate was used (only for the data preparation phase of MuscleNET, not for real-time control).

- **Euler angle data:** A low-pass filter with 30Hz cutoff frequency was used to clear the high-frequency noise of Euler angles measured by IMU components.

- **Motor kinematic data:** To remove the high-frequency noise of the motor velocity $\dot{\phi}_f$ calculated as the numerical derivative of the joint angle, a low-pass filter with 20Hz cutoff frequency was used. The joint angle of the motor ϕ_f was used without any data adjustment.

3. Hierarchical controllers

As shown in Figure 5, the wearable device controller adopts a hierarchical control architecture (Nasr et al., 2021c), which consists of (I) high, (II) mid, and (III) low-level units. [label = .]

I. The high-level unit estimates the user's state and predicts the user's motion or wrench intent (Nasr et al., 2020, 2021a). Researchers are working on developing automated estimation and prediction systems that use machine-learning models and information from IMUs and sEMG wearable sensors. This is in contrast to commercial devices, which use direct manual commands from the user for decision-making tasks (Nasr et al., 2021c). Here, we are using a machine-learning model from Nasr et al. (Nasr et al., 2021a) to estimate the user intent from the IMU and sEMG sensors.

II. The mid-level unit transforms the high-level estimation and prediction into mode-specific reference trajectories, or the desired wrench, using the biomechatronic system's dynamic equations. In the past, this level of control was achieved using a conventional control method: finite state machines/prerecorded motion (Long et al., 2017), master–slave (Lee et al., 2012), proportional (Tang et al., 2014), CTM (Nasr et al., 2022b), fuzzy-logic (Han et al., 2021; Nasr et al., 2022b), impedance control (Brahmi et al., 2021), haptic/admittance control (Menga and Ghirardi, 2019), or adaptive control (Nasiri et al., 2021). Recently, positive results for the mid-level controller have been demonstrated using the AAN-CTM approach, which augments rather than replaces muscular activity (Nasr et al., 2022b).

III. The low-level agent computes the error between the measured states (from the kinematic and kinetic sensors) and the desired device states (from the mid-level controller) and uses common
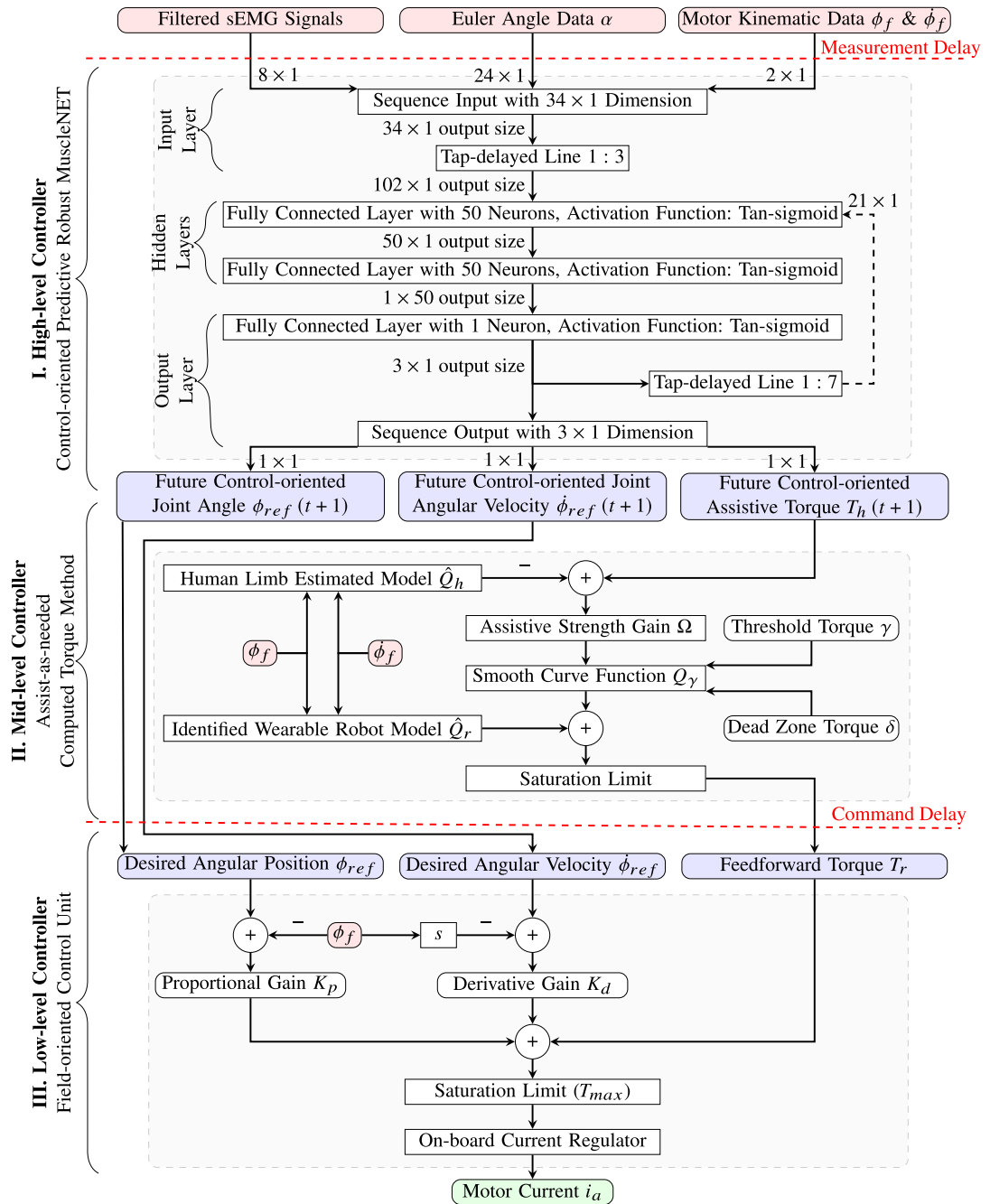
Figure 5. *Block diagram of the hierarchical control architecture of the active–passive exoskeleton robot, including high, mid, and low-level controllers. The high-level unit estimates the future values of the control-oriented joint angle, angular velocity, and assistive torque (Nasr et al., 2023b). The mid-level controller defines the potential driving torque using the human and exoskeleton model. The low-level controller ensures the commanded data matches the motor states.*

control algorithms like proportional-integral-derivative (PID) control. It then instructs the robotic actuators to use reference tracking and closed-loop feedback control to minimize the error (Nasr et al., 2021c).

The controllers for each level are described in the following sections.

3.1. High-level controller

The machine-learning model used here as the high-level controller is called MuscleNET, and its configuration is optimized for mapping IMU and sEMG to kinematic and kinetic biomechanical signals (Nasr et al., 2021a). The fact that muscle dynamics and joint motions rely on motion history is the reason why a recurrent neural network (RNN) is used instead of other feed-forward methods (Barron et al., 2020; Nasr et al., 2021a). Here, the configuration, input, and output data, and training method are described.

The input of the RNN is a fusion of three types of signals: muscle activation from filtered sEMG, Euler angles from IMU, and the exoskeleton joint angle (and its derivative to define joint angular velocity) by built-in angle position sensors. The output of the RNN consists of future control-oriented data that is required for the mid and low-level units.

An RNN (shown on top of Figure 5) has a 34×1 dimensional input (8 filtered sEMG, 24 Euler angle α, 1 motor angle ϕ_f, and 1 motor velocity $\dot{\phi}_f$ data), a 3×1 dimensional output (1 future control-oriented joint angle $\phi_{ref}(t+1)$, 1 future control-oriented joint angular velocity $\dot{\phi}_{ref}(t+1)$, and 1 future control-oriented assistive torque $T_h(t+1)$). The RNN configuration consists of 3 input signal former values and 7 output signal former values. The RNN has 2 hidden layers with 50 nodes having hyperbolic tangent sigmoid activation functions, and the output layer has one neuron with a hyperbolic tangent sigmoid activation function. More information on the data dimensionalities and structures is provided at the top of Figure 5.

A time-shifting technique and dynamic model-based optimization loops were used to prepare the output training data. The motor joint angle and velocity are time-shifted in order to find two of the output training data ($\phi_{ref}(t+1)$ and $\dot{\phi}_{ref}(t+1)$). In addition, the last output training data ($T_h(t+1)$) was calculated using a validated exoskeleton and human musculoskeletal (MSK) model (Nasr et al., 2023a) and an optimization loop. The optimization loop tries to find the actuator's assistive torque (T_h) to decrease the human joint torque (τ_h) (Nasr et al., 2022a; 2023a).

Once the data is gathered from the participant and processed as mentioned, it is then used to train the RNN. Levenberg–Marquardt backpropagation was used as the training method and 2000 was chosen as the maximum epoch. Six hours was set to be the most time that could pass. When doing regression tasks, the half mean squared normalized error (MSE) operation in Equation (1), which calculates the half MSE loss between network predictions and target values, was used to calculate the loss in the model gradient function:

$$loss = \frac{1}{2N}\Sigma_{i=1}^{M}(Y_i - T_i)^2 \tag{1}$$

where

- Y_i is the neural network prediction output,
- T_i is the output target value,
- M is the total number of responses across all observations, and
- N is the total number of observations in Y.

3.2. Mid-level controller

Here, we consider the complete AAN-CTM strategy intended to deliver the necessary assistance torque. This novel method determines the desired actuator torque (T_r) by magnifying the human active torque (τ_h) using the desired strength variable (Ω), and integrating the powered actuator model for the robot in

Equation (2). In the presence of low human joint torque, the hyperbolic Equation (3) eliminates the controller chattering effect. The exoskeleton dynamic model of actuator torque (Q_r) is presented in Equation (4), and sums with the desired torque to cancel the dynamics of the robot structure and the actuator:

$$T_r = \Omega Q_\gamma \left(T_h - \widehat{Q}_h \right) + \widehat{Q}_r \tag{2}$$

$$Q_\gamma = \left| \frac{1}{1 + e^{-\frac{4}{\gamma-\delta}\left(T_h - \frac{\gamma+\delta}{2}\right)}} - \frac{1}{1 + e^{\frac{4}{\gamma-\delta}\left(T_h + \frac{\gamma+\delta}{2}\right)}} \right| \tag{3}$$

$$\widehat{Q}_r = N^2 \widehat{I}_m \ddot{\phi}_f + N^2 \widehat{b}_m \dot{\phi}_f + \widehat{m}_r g \widehat{d}_{com} \sin\left(\phi_f\right) \tag{4}$$

where

T_r is desired/feedforward assistive torque,
T_h is control-oriented assistive elevation torque by the high-level controller,
$\widehat{Q}_h$ is human limb estimated model,
Ω is robot's desired strength variable, which is positive for assistive and negative for resistive control between 0 and∞,
Q_γ is smooth curve of the human elevation torque between the dead zone and the threshold torque,
$\widehat{Q}_r$ is wearable robot actuator model, the result of the rotor inertia and the viscous damping,
γ is the positive threshold torque,
δ is the positive dead zone torque,
ϕ_f is actuator joint angle,
$\dot{\phi}_f$ is actuator joint angular velocity that is calculated with the derivative of the joint angle,
$\ddot{\phi}_f$ is actuator joint angular acceleration that is calculated with the derivative of the joint angular velocity,
N is the gear ratio,
I_m is moment of inertia of the motor rotor around the elevation joint,
b_m is rotator viscous friction coefficient,
$\widehat{m}_r$ is combined mass of the exoskeleton elevation mechanism, housing, and fixture of the motor,
g is gravitational acceleration, and
$\widehat{d}_{com}$ is distance of mass center from the rotational joint.

3.3. Low-level controller

Here we used proportional-derivative (PD)-based and feed-forward controllers adopted from (Katz et al., 2019), and provided in Equation (5). The maximum motor nominal torque limits the desired assistive output torque in Equation (6). A motor's torque-producing ability relevant to its current is usually expressed as Equation (7).

$$T = K_p \left(\phi_{ref} - \phi_f \right) + K_d \left(\dot{\phi}_{ref} - \dot{\phi}_f \right) + T_r \tag{5}$$

$$\overline{T} = min(max(T, -T_{max}), T_{max}) \tag{6}$$

$$i_a = \frac{\overline{T}}{N K_m} \tag{7}$$

where

T_{max} is the maximum nominal motor torque,
$\overline{T}$ is the actual motor torque,
k_m is the motor torque constant, and
i_a is the armature commanded current.

Since the angular velocity is calculated using the first numerical derivative of the joint angle and it has no filter in the FOC, the controller is consequently noisy. Thus, it is reasonable to have a small K_d for a robust controller, but it should nonetheless be more than zero to inhibit any small speed errors. As the proportional gain K_p increases, the robot controller acts as a motion controller, and as it decreases, it acts as a torque controller.

4. Participants and test protocol

- **Participants:** 21 participants (12 male and 9 female; 25 ± 3.2 years; 64 ± 12.9 kg mass; 1.75 ± 0.09 m height; 2.5 ± 1.9 workout session per week; 15 right-handed and 5 left-handed) free of upper extremity injury gave informed consent and performed the following tasks (Figure 6) in different phases. The test protocol has been given ethics clearance by the Research Ethics Board of the University of Waterloo (REB: #43980).
- **Phases:** Participants did tasks during the phases detailed in Table 3. In the first phase, the participant freely moved their upper arm from the natural pose to overhead, as well as contracted the muscles individually. This data was used for motor home angle calibration and calculating the maximum sEMG signal amplitude. In the second phase, participants made the free motion. The data in this phase was used to optimally calculate the assistive torque (Nasr et al., 2023a) and provide training data for the MuscleNET model (Nasr et al., 2021a). The subject would repeat the task for phases 3–6

Figure 6. *The participant is wearing the active exoskeleton and sensors while doing a weight-lifting task in the sagittal plane.*

Table 3. *The six phases of exoskeleton calibration, data-gathering, and test protocol*

Phase	Name	Exoskeleton Structure	Assistance source Passive	Assistance source Active	Tasks Weight lifting	Tasks Free motion
1	Sensor calibration	√				√
2	Data-gathering	√			√	√
3	Inactive exoskeleton	√			√	
4	Fully passive	√	√		√	
5	Active–passive	√	√	√	√	
6	Fully active	√		√	√	

to assess the different sources of assistance (inactive/none, fully passive, fully active, and active–passive assistance).

- **Tasks:** Participants performed two tasks of weight lifting and free motion in the sagittal plane: (1) while wearing the exoskeleton and (2) not wearing the exoskeleton. For the weight lifting task, participants lifted a 2.26kg dumbbell off a stool to about a 90° elevation angle for the shoulder joint. The participants kept the weight at the shoulder height level until they became fatigued. The duration for tolerating the weight was recorded for each phase. Moreover, in phase one, at which data was gathered for training MuscleNET, participants were requested to keep the elbow angle at 0° or 90°.

5. Evaluation criteria

The main goal of this study was to compare the performance of the active–passive exoskeleton with the traditional passive or active exoskeleton. To this end, we applied the following three methods: survey questionnaire, experimental data, and computed data. For the computational criteria, we used the MapleSim Biomechanics (scalable MSK) model, which was developed and validated using experimental dynamometer data (Nasr et al., 2023c).

- **Post-test survey:** This survey aims to determine the user's experience with different actuation situations. Each participant completed a survey relevant to muscle fatigue for each phase once the test had been finished. The user reported the level of fatigue, location of fatigue, and comfort level with the exoskeleton. The results were qualitatively compared.
- **Load tolerance duration:** The participants were required to lift dumbbells as frequently as possible. The duration of this weight tolerance was recorded for phases, and then quantitatively compared.
- **Mean power frequency of initial raw sEMG:** The purpose of the sEMG frequency domain analysis is to detect the variation characteristics via short-fast Fourier transform decomposition of the sEMG signal into signal components at various frequencies. Initial sEMG mean power frequency is used to compare muscles in different phases.
- **Average fatigue of motion using sEMG signals:** Muscle fatigue accumulated during motion is given by $\sum_m \int_T \sigma_m^2 dt$, where the square of muscle activations σ is a fatigue measure widely used in neuromechanical models (Ackermann and van den Bogert, 2010; Gillette et al., 2022). Here, sEMG signals are assumed to be the muscle activations.
- **Average computed fatigue of motion using inverse dynamic simulation and static optimization:** Muscle activation can be calculated using the static optimization, the dynamic model's inputs of recorded joint kinematics and external force/weight.
- **Average computed human active torque and absolute power using sEMG signals and Muscle-NET:** The amplitude and pattern of sEMG channels differed for each phase and each participant. In addition to mentioning their pattern difference for each phase, we used the trained machine-learning model, MuscleNET, to estimate the current shoulder elevation torque. In addition to active joint torque, the absolute joint power was calculated and compared.
- **Average computed human joint torque and power using inverse dynamic simulation:** Another method of calculating joint torque and power is using a dynamic model. The joint torque and power can be computed using the recorded joint kinematics and external force/weight as inputs to the dynamic model.
- **Average computed metabolic energy expenditure using muscle torque generators:** The last evaluation benchmark is computed muscles metabolic energy expenditure (MMEE). The MMEE model verified by Kim and Roberts (2015) helps in the performance measurement of human motion. Kim and Roberts (2015) developed a joint-space numerical model of metabolic energy expenditure by merging thermodynamic laws with principles of multibody system dynamics.
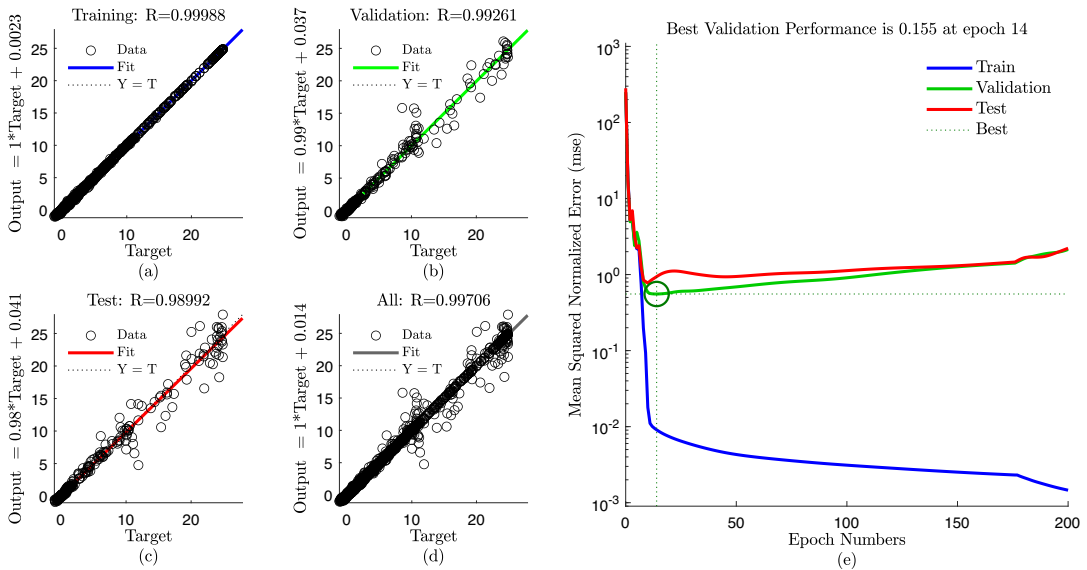
Figure 7. *The regression accuracy of MuscleNET in MSE for (a) training, (b) validation, (c) test, and (d) all data. (e) The training performance of MuscleNET versus epoch number.*

6. Results and discussion

6.1. High-level controller accuracy

We found that the accuracy of the high-level machine-learning model was higher when we used a subject-based model instead of a general model since there were differences between the NMSK of each participant, as highlighted in Nasr et al. (2021a). The accuracy of subject-based MuscleNET for all subjects was more than 99.5%, 99.2%, and 98.9% MSE regression accuracy for training, testing, and validation using randomly separated 70, 15, and 15% of data, respectively (Figure 7(a–d)). Using a variety object weights in the data-gathering phase helps increase the high-level controller's accuracy. However, the tests were limited by the maximum 1-hour battery lifetime of the sEMG sensors and the users exhibited fatigue before the actual exoskeleton test. The best MuscleNET performance occurred with epoch #14 and too much training results in over-fitting (Figure 7(e)).

6.2. Low-level controller gains

Since the participant lifted a weight during their motion, the low-level controller should be more concerned about the assistive torque than the position. In other words, the task was more interested in providing the assistive torque instead of having an accurate tracking error. In addition, the accuracy of the high-level controller is better for future control-oriented assistive torque in comparison to the joint angle and angular velocity. Thus, by trial and error with one of the participants, we determined that the proportional gain (K_p) should be set as small as 5% of the maximum value. Setting the derivative gain (K_d) to a value of 20% of the maximum value helped decrease the actuator's vibration because of the angle tracking error. In total, these gains changed the low-level controller to a direct torque plus a vibration cancellation controller.

6.3. Exoskeleton evaluation

- **Quantitative:** The results of quantitative evaluation criteria are shown in Figures 8 and 9. The criteria for the average of all subjects are shown in the solid bar, as well as the maximum and minimum (Δ and ∇) with the STD (blue line) on the bar charts. According to Figure 8, the most efficient exoskeleton types from weak to powerful are: inactive, fully passive, fully active, and
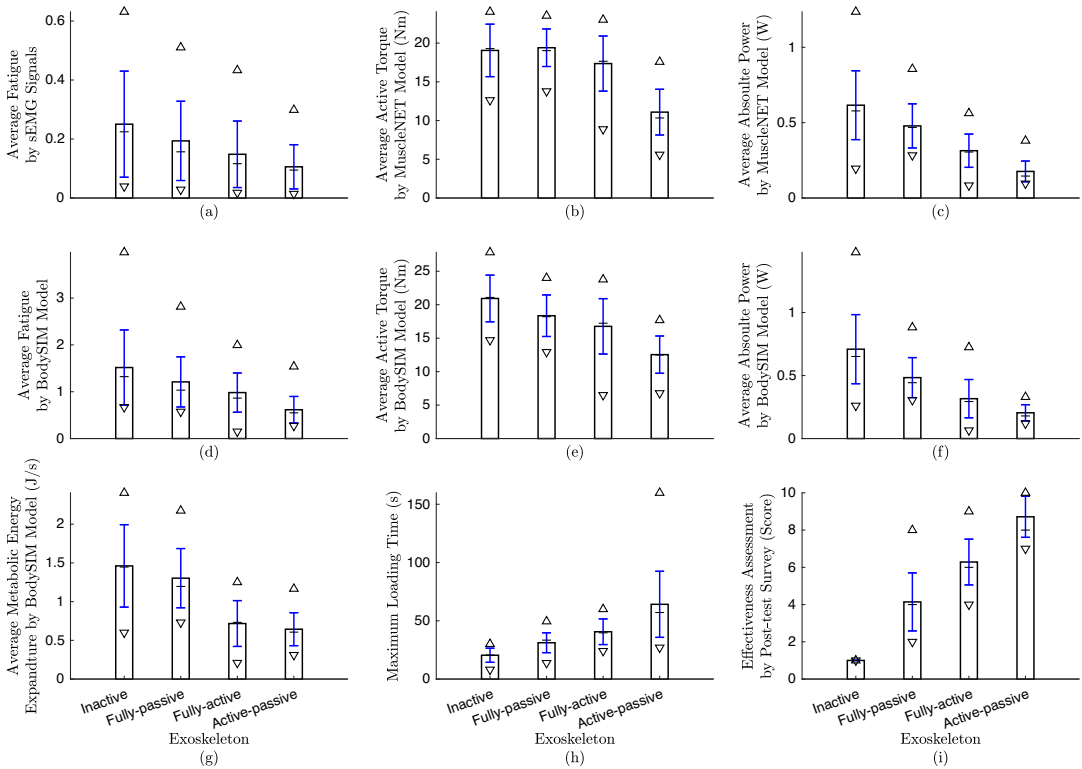
Figure 8. *The quantitative evaluation values for the four exoskeleton actuation types (inactive, fully passive, fully active, and active–passive). Note that the maximum (∆), minimum (∇), median (−), and STD (blue line) are shown on the average of all subjects (bar charts). (a–c) are calculated from sEMG signals; (d–g) are calculated using the inverse dynamic MapleSim Biomechanics model and measured kinematic data. (a & d) shows average fatigue; (b & e) are showing average human flexion active torque; (c & f) shows average absolute power; (g) displays the average muscle energy expenditure; (h) shows the maximum duration time of load tolerance; and (j) displays the result of the post-test personal survey on the effectiveness of the exoskeletons.*

active–passive. According to Figures 9(b), 9(c), 8(a), and 8(d), using the active–passive exoskeleton can decrease the fatigue level compared to using the fully passive exoskeleton.

As seen in Figure 8(h), participants could lift the object for more time until they became fatigued by using the active–passive exoskeleton. The active–passive exoskeleton can be helpful for almost 2 times longer than the fully passive exoskeleton. In fact, the active–passive exoskeleton is adaptive to the task and can provide variable assistive torque instantly, as compared to the fully passive torque that can only provide fixed assistive torque at one specific angle, as mentioned in Nasr et al. (2022a). The participants scored the active–passive exoskeleton to be more effective than other exoskeletons (Figure 8(j)).

For the majority of muscles, according to Figures 9(a, b, and d), the muscles were activated, the median frequency was decreased, and the median power was increased from low to high for the following exoskeletons: active–passive, fully active, fully passive, and inactive. This means that the muscles became less fatigued with the active–passive exoskeleton. However, a couple of muscles showed not to have similar trends with most of the other muscles. For example, the sEMG signals from the BRD location showed no signs of fatigue. Obviously, BRD is for elbow flexion/extension (EFE), and the exoskeleton had no effect on these muscles and joints.
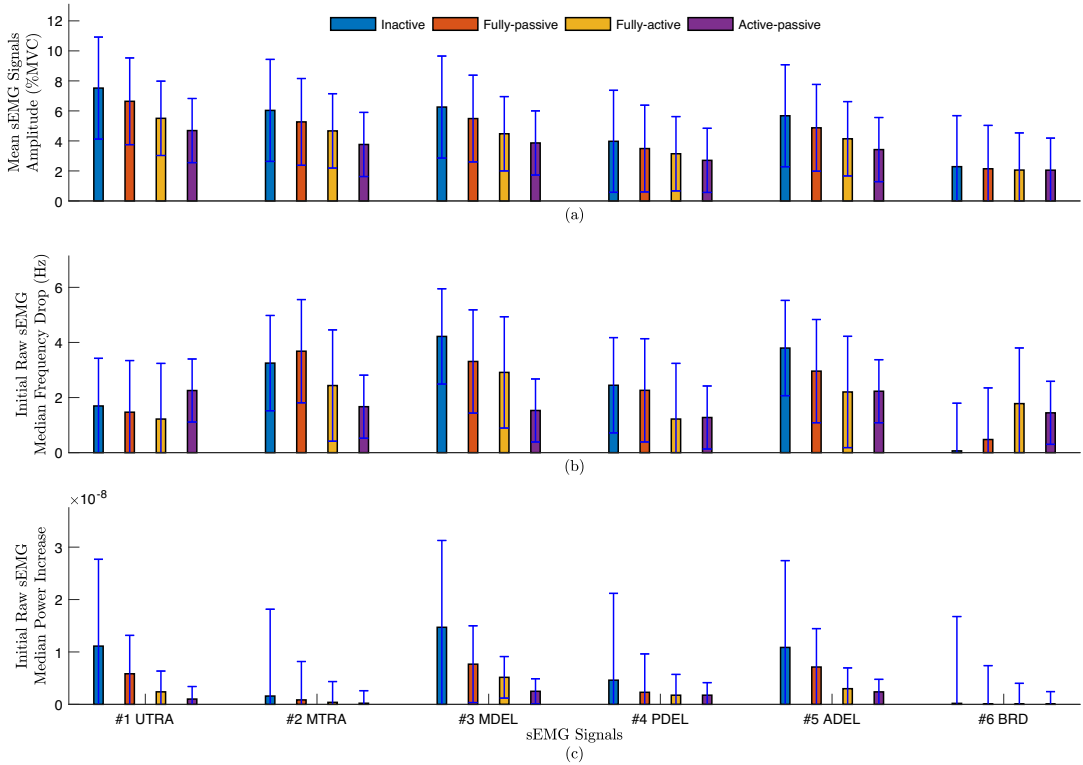
Figure 9. *The muscle fatigue evaluations for the four exoskeleton actuation types (inactive, fully passive, fully active, and active–passive). (a) Mean sEMG signals amplitude percentage; (b & c) Mean frequency drop and power increase of initial raw sEMG signal. The STD (blue line) is also shown on the average of all subjects (bar charts).*

- **Qualitative:** All participants ranked the active–passive exoskeleton double that of the fully passive exoskeleton and 1.5 times that of the fully active exoskeleton. They stated the following sentences for the active–passive ones in the post-test survey: "I feel my arm was on a table and became less fatigued." "The active–passive was much more helpful than other kinds." "I feel it was holding my arm and had no shoulder pain and fatigue with active–passive and finished the experiment because of my elbow fatigue." "The active–passive phase was significantly effective, and I finished due to wrist fatigue." "I feel I was completely at rest and could hold the object longer." "Felt good and no interference. Overall it was pretty smooth."

6.4. sEMG-based control

A sample of the active–passive exoskeleton test is shown in Figure 10. The raw measured and filtered sEMG signals are shown at Figure 10(a–f). The predicted joint angle, angular velocity, and the human joint torque contribution to the motion by MuscleNET, as well as the measured and post-calculated values, are shown in Figure 10(m–o). The exoskeleton's passive torque, the commanded torque, and total torque are shown in Figure 10(p–r). The mid-level AAN-CTM controller defined the active torque according to the human contribution.

As observed in Figure 10, the volitional control of the active component was successful. However, one minor challenge was the time delay when the participants wanted to lower their arm at the end of each
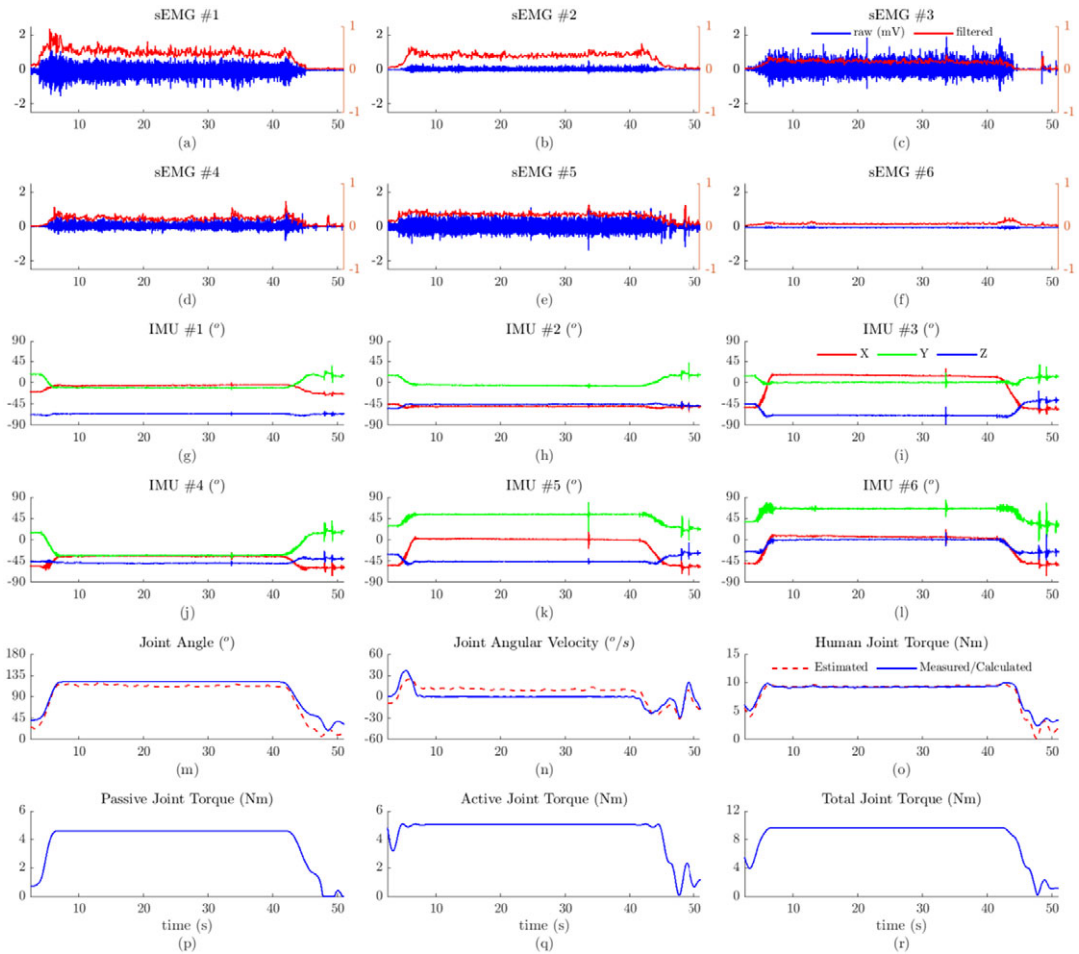
Figure 10. *A sample of raw, filtered, estimated, and computed data for active–passive exoskeleton control test. (a–f) the raw and filtered sEMG signals: #1 UTRA, #2 MTRA, #3 MDEL, #4 PDEL, #5 ADEL, and #6 BRD; (g–l) the raw Euler angles measured by IMUs; (m) predicted and measured exoskeleton elevation angle; (n) predicted and measured exoskeleton elevation angular speed; (o) the estimated and calculated human contribution torque for the elevation motion, (p) the passive robot torque, (q) the commanded active robot torque, and (r) the total assisted torque.*

phase, which is discussed in Section 8. In addition, there was a minor error in the calculation of the joint angle, angular velocity, and human joint torque. Nonetheless, the minor human joint torque error was deemed feasible and was considered in designing the mid-level controller with the positive dead zone torque (δ). The hyperbolic Equation (3) successfully ignored minor differences from the estimated human torque and expected human upper-limb dynamic without the external wrench. Basically, Equation (2) strengthens the estimated human joint torque that is higher than the positive threshold torque (γ), and tries to ignore the lower human joint torque than the positive dead zone torque (δ).

7. Practical challenges and future directions

We found the following challenges in the experimental test. Researchers in wearable robotics should address these challenges in the future.

- **Measurement and command delay:** The delay is the main challenge in the HITL experiment. The delay for fetching sEMG and IMU data was 190ms, since the Delsys Trigno wireless is not real-time equipment and is primarily used for recording and offline analysis. The second primary source of delay was BLDC motor communication with the amount of 185ms. The reason is because there are three connection protocols between MATLAB and BLDC motor, as shown in Figure 2. Actually, serial connection, which is responsible for delivering a string or character, is not efficient and fast. This is because once the data is sent from MATLAB to Arduino, it should be converted to a number and then be commanded to the motor. The last delay source is the computation delay with the amount of 90ms. Filtering sEMG signal, using the machine-learning model, using the CTM, calculating the motor communication instruction, and displaying data in MATLAB, are altogether time-consuming tasks and should be optimized or downgraded to a low-level or embedded controller.
- **Sensor fusion:** Although using these different sensors (sEMG, IMU, and joint angle) is helpful for the estimation of human motion and muscle contribution, this process requires synchronization. Any delay in one sensor should be considered in the model, and the sensor fusion scheme should compensate for synchronization problems.
- **Kinematic sensor inaccuracy:** Currently, an incremental-type sensor measures the motor joint angle. The absolute joint angle measurement requires knowing a global value. We asked the participant to hold the arm downward to calibrate the joint angle sensor. As a result, using an accurate absolute joint angle sensor helped cancel the initial home address setting.
- **sEMG probe and motor built-in sensor disconnection:** Sometimes, the sEMG sensors become disconnected due to detachment or power loss due to a weak battery. The onboard motor sensors sometimes disconnected due to differences in the connection band rate. The HITL controller should be robust and safe regarding any sensor disconnections.

8. Conclusion

Exoskeleton robots have become a valuable tool for supporting industrial workers and stroke rehabilitation therapy. The movements of these robots can range from being entirely passive to being fully active-assisted. Due to the complex HRIs, realistic sensor and actuator selection, and connection challenges, evaluating exoskeleton actuation designs and building an efficient controller are different and time-consuming. To execute the wearer's movement goals, this research presented an sEMG-based human-robot cooperative control method. It also established a test framework for evaluating a new active–passive shoulder exoskeleton. A mid-level strength regulation, low-level actuator control, and control-oriented sEMG-based intention estimate were all utilized in the hierarchical control. It was then used to test the controller's efficiency during shoulder joint elevation movement studies with the exoskeleton.

According to the results, the active–passive exoskeleton was more efficient in comparison to the fully passive and fully active exoskeleton with the following evaluation criteria: (1) post-test personal survey, (2) load tolerance duration, and (3) computed human active torque, power, computed metabolic energy expenditure using both sEMG signals and inverse dynamic simulation. The results showed that the active–passive exoskeleton was better than the fully passive and fully active exoskeleton, since the participants could hold the weighted object for about two times longer in duration until they became fatigued.

Future improvements should focus on decreasing the communication delay, and proposing more robust and safe controllers.

Glossary

AAN	assist-as-needed.
ADEL	anterior deltoid.
BLDC	brushless direct current.
BRD	brachioradialis.

CAN-bus	controller area network.
CTM	computed-torque method.
DoF	degree of freedom.
EFE	elbow flexion/extension.
FOC	field-oriented control.
HITL	human-in-the-loop.
HRI	human–robot interaction.
IMU	inertial measurement unit.
MDEL	middle deltoid.
MMEE	muscles metabolic energy expenditure.
MSE	mean squared normalized error.
MSK	musculoskeletal.
MTRA	middle trapezius.
MuscleNET	machine-learning mapping electromyography to kinematic and dynamic biomechanical variables.
NMSK	neuromusculoskeletal.
PD	proportional-derivative.
PDEL	posterior deltoid.
PID	proportional-integral-derivative.
RNN	recurrent neural network.
SDK	software development toolkit.
sEMG	surface electromyography.
SPI	serial peripheral interface.
STD	Standard deviation.
TCP	transmission control protocol.
TCU	trigno control utility.
UTRA	upper trapezius.

References

Ackermann M and van den Bogert AJ (2010). Optimality principles for model-based prediction of human gait. *Journal of Biomechanics* **43**(6), 1055–1060. https://doi.org/10.1016/j.jbiomech.2009.12.012

Al-Hayali NK, **Chiad JS**, **Nacy SM and Hussein O** (2021a). A review of passive and quasi-passive lower limb exoskeletons for gait rehabilitation. *Journal of Mechanical Engineering Research and Developments* **44**(9), 436–447.

Al-Hayali NK, **Nacy SM**, **Chiad JS and Hussein O** (2021b). Analysis and evaluation of a quasi-passive lower limb exoskeleton for gait rehabilitation. *Al-Khwarizmi Engineering Journal* **17**(4), 36–47. https://doi.org/10.22153/kej.2021.12.007

Asl HJ, **Katagiri K**, **Narikiyo T**, **Yamashita M and Kawanishi M** (2021). Satisfying task completion and assist-as-needed performance in robotic exoskeletons. *IEEE Transactions on Medical Robotics and Bionics* **3**(3), 791–800. https://doi.org/10.1109/tmrb.2021.3097132

Bai S, **Islam MRU**, **Hansen K**, **Nørgaard J**, **Chen CY and Yang G** (2022). A semi-active upper-body exoskeleton for motion assistance. *Biosystems and Biorobotics* **27**, 301–305. https://doi.org/10.1007/978-3-030-69547-7_49

Barron O, **Raison M**, **Gaudet G and Achiche S** (2020). Recurrent neural network for electromyographic gesture recognition in transhumeral amputees. *Applied Soft Computing Journal* **96**, 106616. https://doi.org/10.1016/j.asoc.2020.106616

Blanchet L, **Achiche S**, **Docquier Q**, **Fisette P and Raison M** (2020). A procedure to optimize the geometric and dynamic designs of assistive upper limb exoskeletons. *Multibody System Dynamics* **51**(2), 221–245. https://doi.org/10.1007/s11044-020-09766-6

Bogue R (2018). Exoskeletons – A review of industrial applications. *Industrial Robot* **45**(5), 585–590. https://doi.org/10.1108/IR-05-2018-0109

Brahmi B, **Driscoll M**, **El Bojairami IK**, **Saad M and Brahmi A** (2021). Novel adaptive impedance control for exoskeleton robot for rehabilitation using a nonlinear time-delay disturbance observer. *ISA Transactions* **108**, 381–392. https://doi.org/10.1016/j.isatra.2020.08.036

de Looze MP, **Bosch T**, **Krause F**, **Stadler KS and O'Sullivan LW** (2016). Exoskeletons for industrial application and their potential effects on physical work load. *Ergonomics* **59**(5), 671–681. https://doi.org/10.1080/00140139.2015.1081988

de Vries AW and de Looze MP (2019). The effect of arm support exoskeletons in realistic work activities: A review study. *Journal of Ergonomics* **9**(4), 1–9. https://doi.org/10.35248/2165-7556.19.9.255

Di Natali C, **Sadeghi A**, **Mondini A**, **Bottenberg E**, **Hartigan B**, **De Eyto A**, **O'Sullivan L**, **Rocon E**, **Stadler K**, **Mazzolai B**, **Caldwell DG and Ortiz J** (2020). Pneumatic quasi-passive actuation for soft assistive lower limbs exoskeleton. *Frontiers in Neurorobotics* **14**, 31. https://doi.org/10.3389/fnbot.2020.00031

Drake JD and Callaghan JP (2006). Elimination of electrocardiogram contamination from electromyogram signals: An evaluation of currently used removal techniques. *Journal of Electromyography and Kinesiology* **16**(2), 175–187. https://doi.org/10.1016/j.jelekin.2005.07.003

du Plessis T, **Djouani K and Oosthuizen C** (2021). A review of active hand exoskeletons for rehabilitation and assistance. *Robotics* **10**(1), 5351–5356. https://doi.org/10.3390/robotics10010040

Fritzsche L, **Galibarov PE**, **Gärtner C**, **Bornmann J**, **Damsgaard M**, **Wall R**, **Schirrmeister B**, **Gonzalez-Vargas J**, **Pucci D and Maurice P** (2021). Assessing the efficiency of exoskeletons in physical strain reduction by biomechanical simulation with AnyBody modeling system. *Wearable Technologies* **2**, e6. https://doi.org/10.1017/wtc.2021.5

Gillette JC, **Saadat S and Butler T** (2022). Electromyography-based fatigue assessment of an upper body exoskeleton during automotive assembly. *Wearable Technologies* **3**, e23. https://doi.org/10.1017/wtc.2022.20

Gopura R, **Bandara DSV**, **Kiguchi K and Mann GKI** (2016). Developments in hardware systems of active upper-limb exoskeleton robots: A review. *Robotics and Autonomous Systems* **75**, 203–220. https://doi.org/10.1016/j.robot.2015.10.001

Gull MA, **Bai S and Bak T** (2020). A review on design of upper limb exoskeletons. *Robotics* **9**(1), 16. https://doi.org/10.3390/robotics9010016

Han J, **Yang S**, **Xia L and Chen YH** (2021). Deterministic adaptive robust control with a novel optimal gain design approach for a fuzzy 2-DOF lower limb exoskeleton robot system. *IEEE Transactions on Fuzzy Systems* **29**(8), 2373–2387. https://doi.org/10.1109/TFUZZ.2020.2999739

Hassan Z and Sadik W (2018). Design quasi passive exoskeleton for below knee prosthesis. *Journal of Engineering and Applied Sciences* **13**(23), 8994–9001.

Hermens HJ, **Freriks B**, **Disselhorst-Klug C and Rau G** (2000). Development of recommendations for sEMG sensors and sensor placement procedures. *Journal of Electromyography and Kinesiology* **10**(5), 361–374. https://doi.org/10.1016/S1050-6411(00)00027-4

Hislop H, **Avers D and Brown M** (2013). *Daniels and Worthingham's Muscle Testing: Techniques of Manual Examination and Performance Testing*. St. Louis, MO, USA: Elsevier.

Jamsek M, **Petric T and Babix J** (2020). Gaussian mixture models for control of quasi-passive spinal exoskeletons. *Sensors* **20**(9), 2705. https://doi.org/10.3390/s20092705

Katz B, **Carlo JD and Kim S** (2019). Mini cheetah: A platform for pushing the limits of dynamic quadruped control. In *Proceedings of the IEEE International Conference on Robotics and Automation, 2019-May*. Montreal, QC: IEEE, pp. 6295–6301. https://doi.org/10.1109/ICRA.2019.8793865

Kim JH and Roberts D (2015). A joint-space numerical model of metabolic energy expenditure for human multibody dynamic system. *International Journal for Numerical Methods in Biomedical Engineering* **31**(9), e02721. https://doi.org/10.1002/cnm.2721

Lambrecht BG and Kazerooni H (2009). Design of a semi-active knee prosthesis. In *Proceedings of the IEEE International Conference on Robotics and Automation*. Kobe, Japan: IEEE, pp. 639–645.

Lee HD, **Kim WS**, **Han JS and Han CS** (2012). The technical trend of the exoskeleton robot system for human power assistance. *International Journal of Precision Engineering and Manufacturing* **13**(8), 1491–1497. https://doi.org/10.1007/s12541-012-0197-x

Long Y, **Du Z**, **Cong L**, **Wang W**, **Zhang Z and Dong W** (2017). Active disturbance rejection control based human gait tracking for lower extremity rehabilitation exoskeleton. *ISA Transactions* **67**, 389–397. https://doi.org/10.1016/j.isatra.2017.01.006

Matthew RP, **Mica EJ**, **Meinhold W**, **Loeza JA**, **Tomizuka M and Bajcsy R** (2015). Introduction and initial exploration of an active/passive exoskeleton framework for portable assistance. In *Proceedings of the IEEE International Conference on Intelligent Robots and Systems*, vol. 2015. Hamburg, Germany: IEEE, pp. 5351–5356.

Menga G and Ghirardi M (2019). Control of the sit-to-stand transfer of a biped robotic device for postural rehabilitation. *Robotics* **8**(4), 91. https://doi.org/10.3390/ROBOTICS8040091

Miakovic L, **Dezman M and Petric T** (2022). Modular quasi-passive mechanism for energy storage applications: Towards lightweight high-performance exoskeleton. In *Proceedings of the 20th International Conference on Advanced Robotics*. Ljubljana, Slovenia: IEEE, pp. 588–593.

Naito J, **Nakayama A**, **Obinata G and Hase K** (2007). Development of a wearable robot for assisting carpentry workers. *International Journal of Advanced Robotic Systems* **4**(4), 48. https://doi.org/10.5772/5667

Nasiri R, **Shushtari M and Arami A** (2021). An adaptive assistance controller to optimize the exoskeleton contribution in rehabilitation. *Robotics* **10**(3), 95. https://doi.org/10.3390/robotics10030095

Nasr A, **Bell S**, **He J**, **Whittaker RL**, **Jiang N**, **Dickerson CR and McPhee J** (2021a). MuscleNET: Mapping electromyography to kinematic and dynamic biomechanical variables. *Journal of Neural Engineering* **18**(4), 0460d3. https://doi.org/10.1088/1741-2552/ac1adc

Nasr A, **Bell S and McPhee J** (2023a). Optimal design of active-passive shoulder exoskeletons: A computational modeling of human-robot interaction. *Multibody System Dynamics* **57**, 73–106. https://doi.org/10.1007/s11044-022-09855-8

Nasr A, **Bell S**, **Whittaker RL**, **Dickerson CR and McPhee J** (2023b). Robust machine learning mapping of sEMG signals to future actuator commands in biomechatronic devices. *Journal of Bionic Engineering*.

Nasr A, **Ferguson S and McPhee J** (2022a). Model-based design and optimization of passive shoulder exoskeletons. *Journal of Computational and Nonlinear Dynamics* **17**(5), 051004. https://doi.org/10.1115/1.4053405

Nasr A, **Hashemi A and McPhee J** (2022b). Model-based mid-level regulation for assist-as-needed hierarchical control of wearable robots: A computational study of human-robot adaptation. *Robotics* **11**(1), 20. https://doi.org/10.3390/robotics11010020

Nasr A, **Hashemi A and McPhee J** (2023c). Scalable musculoskeletal model for dynamic simulations of upper body movement. *Computer Methods in Biomechanics and Biomedical Engineering*, 1–32. https://doi.org/10.1080/10255842.2023.2184747

Nasr A, **He J**, **Jiang N and McPhee J** (2020). Activation torque estimation of muscles by forward neural networks (Forward-MuscleNET) for sEMG-based control of assistive robots. In *Proceedings of the 7th International Conference of Control, Dynamic Systems, and Robotics. Virtual Conference*. Avestia Publishing, pp. 146.

Nasr A, **He J**, **Jiang N and McPhee J** (2021b). Muscle modelling using machine learning and optimal filtering of sEMG signals. In *Proceedings of the 45th Meeting of the American Society of Biomechanics*. Virtual, pp. 83.

Nasr A, **Laschowski B and McPhee J** (2021c). Myoelectric control of robotic leg prostheses and exoskeletons: A review. In *Proceedings of the ASME International Design Engineering Technical Conferences & Computers and Information in Engineering Conference*, vol. 85444. ASME.

Neto OP and Christou EA (2010). Rectification of the EMG signal impairs the identification of oscillatory input to the muscle. *Journal of Neurophysiology* **103**(2), 1093–1103. https://doi.org/10.1152/jn.00792.2009

Otten BM, **Weidner R and Argubi-Wollesen A** (2018). Evaluation of a novel active exoskeleton for tasks at or above head level. *IEEE Robotics and Automation Letters* **3**(3), 2408–2415. https://doi.org/10.1109/LRA.2018.2812905

Pillai MV, **Van Engelhoven L and Kazerooni H** (2020). Evaluation of a lower leg support exoskeleton on floor and below hip height panel work. *Human Factors* **62**(3), 489–500. https://doi.org/10.1177/0018720820907752

Reaz MBI, **Hussain S and Mohd-Yasin F** (2006). Techniques of EMG signal analysis: Detection, processing, classification and applications. *Biological Procedures Online* **8**(1), 11–35. https://doi.org/10.1251/bpo115

Ren L, **Cong M**, **Zhang W and Tan Y** (2021). Harvesting the negative work of an active exoskeleton robot to extend its operating duration. *Energy Conversion and Management* **245**, 114640. https://doi.org/10.1016/j.enconman.2021.114640

Smith RL, **Lobo-Prat J**, **Van Der Kooij H and Stienen AH** (2013). Design of a perfect balance system for active upper-extremity exoskeletons. In *Proceedings of the IEEE International Conference on Rehabilitation Robotics*. Seattle, WA, USA: IEEE, pp. 1–6.

Tang Z, **Zhang K**, **Sun S**, **Gao Z**, **Zhang L and Yang Z** (2014). An upper-limb power-assist exoskeleton using proportional myoelectric control. *Sensors* **14**(4), 6677–6694. https://doi.org/10.3390/s140406677

Wang Y, **Wang H and Tian Y** (2021a). Adaptive interaction torque-based AAN control for lower limb rehabilitation exoskeleton. *ISA Transactions* **128**, 184–197. https://doi.org/10.1016/j.isatra.2021.10.009

Wang Z, **Wu X**, **Zhang Y**, **Chen C**, **Liu S**, **Liu Y**, **Peng A and Ma Y** (2021b). A semi-active exoskeleton based on EMGs reduces muscle fatigue when squatting. *Frontiers in Neurorobotics* **15**, 30. https://doi.org/10.3389/fnbot.2021.625479

Winter A, **Mohajer N and Nahavandi D** (2022). Semi-active assistive exoskeleton system for elbow joint. In *Proceedings of the IEEE International Conference on Systems, Man, and Cybernetics*. Melbourne, Australia: IEEE, pp. 2347–2353.

Yihun Y, **Adhikari V**, **Majidirad A and Desai J** (2020). Task-based knee rehabilitation with assist-as-needed control strategy and recovery tracking system. *Journal of Engineering and Science in Medical Diagnostics and Therapy* **3**(2), 19–1051. https://doi.org/10.1115/1.4046400

Young AJ and Ferris DP (2017). State of the art and future directions for lower limb robotic exoskeletons. *IEEE Transactions on Neural Systems and Rehabilitation Engineering* **25**(2), 171–182. https://doi.org/10.1109/TNSRE.2016.2521160

Yun Y, **Na Y**, **Esmatloo P**, **Dancausse S**, **Serrato A**, **Merring CA**, **Agarwal P and Deshpande AD** (2020). Improvement of hand functions of spinal cord injury patients with electromyography-driven hand exoskeleton: A feasibility study. *Wearable Technologies* **1**, e8. https://doi.org/10.1017/wtc.2020.9

Zahedi A, **Wang Y**, **Martinez-Hernandez U and Zhang D** (2021). A wearable elbow exoskeleton for tremor suppression equipped with rotational semi-active actuator. *Mechanical Systems and Signal Processing* **157**, 107674. https://doi.org/10.1016/j.ymssp.2021.107674